

PCDreamer: Point Cloud Completion Through Multi-view Diffusion Priors

Guangshun Wei¹ Yuan Feng¹ Long Ma¹ Chen Wang¹ Yuanfeng Zhou¹ Changjian Li²

¹Shandong University ²University of Edinburgh

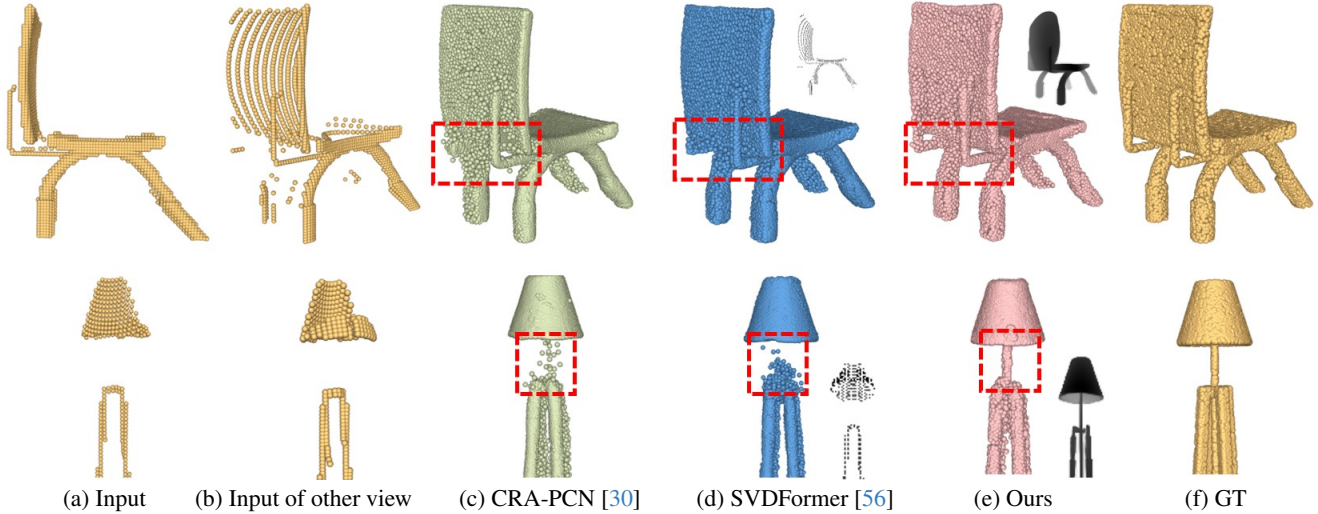


Figure 1. Given a partial point cloud input (a) with (b) as a novel view for visualization purposes, the goal of point cloud completion is to produce a complete point cloud retaining both the global and local geometric features. Existing methods (c, d) fail to neither recover local thin structures (e.g., the lamp holder) nor capture the global symmetric parts (e.g., the back supporter of the chair), while our approach (e) faithfully produces the desired shape compared with the ground truth (f).

Abstract

This paper presents PCDreamer, a novel method for point cloud completion. Traditional methods typically extract features from partial point clouds to predict missing regions, but the large solution space often leads to unsatisfactory results. More recent approaches have started to use images as extra guidance, effectively improving performance, but obtaining paired data of images and partial point clouds is challenging in practice. To overcome these limitations, we harness the relatively view-consistent multi-view diffusion priors within large models, to generate novel views of the desired shape. The resulting image set encodes both global and local shape cues, which is especially beneficial for shape completion. To fully exploit the priors, we have designed a shape fusion module for producing an initial complete shape from multi-modality input (i.e., images and point clouds), and a follow-up shape consolidation module to obtain the final complete shape by discarding unreliable points introduced by the inconsistency from diffusion priors. Extensive experimental results demonstrate our supe-

rior performance, especially in recovering fine details.

1. Introduction

Point cloud completion plays a pivotal role in the advancement of 3D vision, serving as a crucial step in numerous applications, including autonomous driving [17, 29], robotics [4, 36], and augmented reality [10]. Incomplete point clouds, often resulting from scanning occlusions or limited sensor range, pose significant challenges. Although many encouraging approaches [6, 15, 30, 33, 40, 41, 43–45, 48, 49, 51, 55, 56] have been proposed, there is still considerable room for improvement regarding global completeness and local geometric details of resulting point clouds.

This paper addresses this task, focusing on single-view partial point clouds with self-occlusion [6, 15, 30, 33, 40, 43–45, 48, 49, 55]. As shown in Fig. 1(a) and (b), due to the single-view nature of the scanning process, the self-occlusion often leads to the loss of more than half of the 3D shape. Typical cases, like the lamp without the whole backside and the chair without most of the right side of the seat and legs, are shown in Fig. 1. The big missing region

implies a vast solution space for completion.

Most existing methods [6, 30, 55, 56] rely solely on geometric information from partial point clouds to generate a complete shape in a coarse-to-fine manner. Although lacking the symmetric supporter of the chair back (Fig. 1(c)), the overall chair shape is completed with a certain amount of detail. However, the partial lamp without the critical top holder fails those methods, resulting in a random local guess. To address this, some approaches [1, 41, 51, 56] incorporate additional image information to improve completeness (Fig. 1(d), the chair), but obtaining paired image data is challenging in practice.

Motivated by the success of diffusion-based image generation [23, 25], we observe that the relatively view-consistent multi-view images generated by large diffusion models provide rich global and local shape cues, which are particularly advantageous for shape completion. For instance, when conditioned on partial point clouds, the generated images capture symmetric elements, such as the back of the chair (Fig. 1(e) top) and the top holder of the lamp (Fig. 1(e) bottom), enabling the full shape completion with all relevant features.

To harness the diffusion priors, we propose *PCDreamer*, a novel algorithm composed of three key components for high-quality point cloud completion. We, for the first time, introduce diffusion priors in this task. Specifically, in the first module, given the single-view partial point cloud, we utilize a large multi-view diffusion model to ‘dream’ a set of realistic images *for free*. These multi-view images depict the desired shape, serving as the fuel for the completion. The second module employs the attention mechanism to effectively fuse both the images and partial point cloud observation, leading to an initial full shape that preserves both the global structure and local features. Additionally, to address the inconsistency introduced by the multi-view images, the final module incorporates a confidence-guided shape consolidator, which produces the final complete shape with high fidelity. Extensive evaluation and experiments demonstrate the superior performance of our approach.

2. Related Work

Partial point cloud-based shape completion. Point cloud completion has traditionally relied on partial point clouds, often using intermediate 3D representations processed by 3D convolution, which suffer from resolution limits and high computational costs [8, 11, 32, 36]. Point-based networks like PointNet [26, 27] emerged to process 3D coordinates directly, with PCN [49] being the first to use an end-to-end point-based approach, generating points through coarse-to-fine folding. Subsequent encoder-decoder methods [22, 37, 40, 43] improved performance.

Recent attention-based approaches, particularly those using vector attention mechanisms [53], have further ad-

vanced the field. SnowflakeNet [43] and CRA-PCN [30] introduced novel transformer-based components for improved detail generation. SeedFormer [55] and AnchorFormer [6] both predict shape representations that preserve local information and integrate these representations into the generation process to restore high-fidelity details. Methods like PoinTr [48] use the partial point cloud as a condition, leveraging Transformer architectures to predict missing points. Despite the improvements, Transformer-based approaches still struggle with severely incomplete point clouds due to limited supplementary information.

Partial point cloud & Images-based shape completion.

Given the limited geometric information in partial point clouds, other approaches incorporate additional data like RGB images and depth images to enhance completion performance. MVCN [14] uses a conditional GAN for completion in the 2D domain by leveraging rendered depth images from 3D shapes, but this results in spatial information loss. ViPC [51] addresses this by combining partial point clouds with single-view RGB images, though RGB images alone provide insufficient spatial detail. Similarly, Cross-PCC [41] employs single-view RGB images and 2D depth images from complete objects, achieving unsupervised point cloud completion without requiring full 3D point clouds. SVDFormer [56] utilizes multi-view depth images from partial point clouds to generate global shapes and produce new points by incorporating learned shape priors and geometric information. However, these depth images, though containing some spatial information, lack comprehensive geometric priors.

Multi-view images generation. Early works [24, 31, 35] employed specialized attention mechanisms to facilitate cross-view interactions, but often struggled with achieving fine detail consistency and incurred high computational costs. Wonder3D [25] tackled these limitations using a diffusion model equipped with cross-domain attention to generate both multi-view images and normal images. More recent approaches [13, 16, 19, 28, 39] have enhanced generation quality by incorporating novel attention mechanisms and generating multiple modalities.

Video generation presents even greater challenges due to the need for maintaining temporal consistency. Unlike previous methods [3, 9, 12, 18, 52, 54], Stable Video Diffusion [2] introduces a strategy of fine-tuning the entire video diffusion model, rather than focusing solely on temporal layers. This approach provides strong multi-view 3D priors, significantly improving cross-view consistency and generalization, and achieving superior results compared to image-based methods.

3. Method

Given a partial, non-uniform point cloud $P_{in} \in \mathbb{R}^{N \times 3}$, our goal is to produce a dense, uniform, and complete point

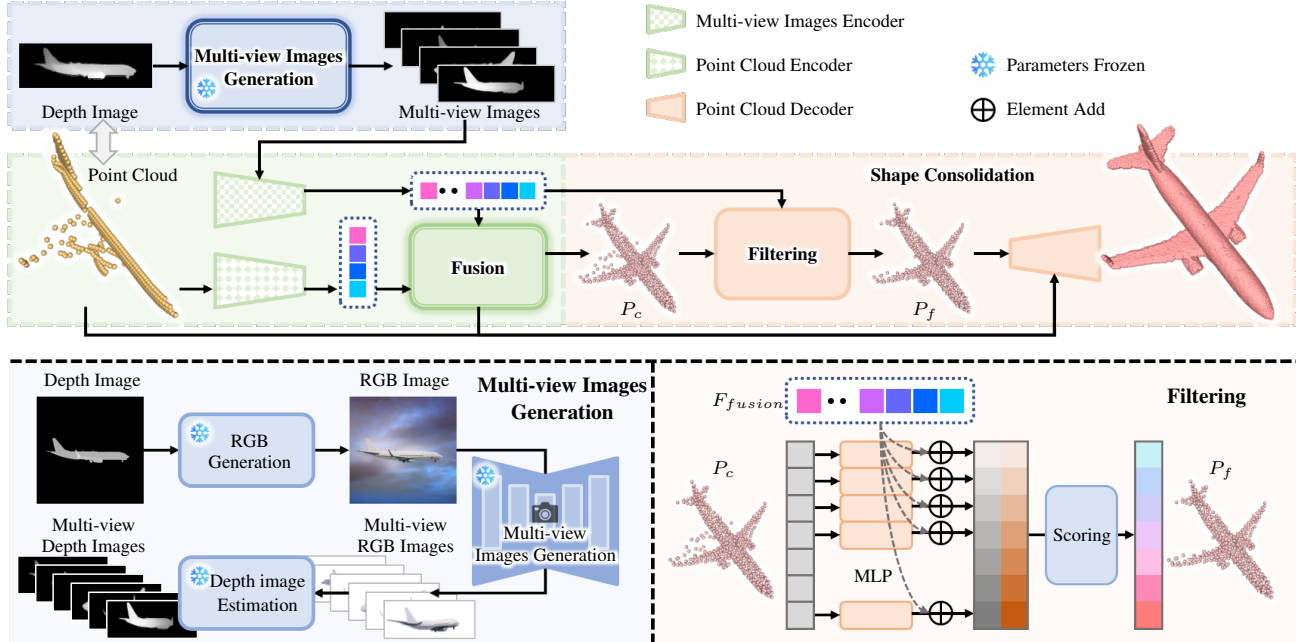


Figure 2. **Overview of PCDreamer.** Given an input partial point cloud, we have designed three core modules to complete it. The multi-view image generation module (Sec. 3.1) *dreams* out multi-view images of the input by leveraging a few large models. The priors within these models serve as the fuel for the completion. The following fusion module (Sec. 3.2) effectively fuses the original input and the inspiring MV images with the help of the attention mechanism. A final consideration module (Sec. 3.3) further reduces the inherent inconsistency introduced in large models, producing a complete, dense, and uniform point cloud with both the global and local shape features.

cloud $P_r \in \mathbb{R}^{RN \times 3}$ that preserves a consistent global shape while retaining detailed local features. Fig. 2 provides an overview of our method consisting of three core components, *i.e.*, multi-view image generation, multi-modality shape fusion, and shape consolidation. In the following, we elaborate on the details.

3.1. Multi-view Image Generation

Given a partial point cloud observation, we aim to ‘dream’ out the full shape. To this end, we resort to the large multi-view diffusion models. There are a few choices for multi-view generation. For instance, RichDreamer [28] can conditionally generate multi-view depth images. However, the resulting images are of low resolution and poor consistency. To the best of our knowledge, no existing large model is capable of fulfilling this specific purpose. We thus designed a pipeline composed of a few large models in place (Fig. 2, bottom left).

Since most of the multi-view diffusion models take as input an RGB image, we first employ ControlNet [50] to translate the single-view depth image into an RGB image. We then pass the RGB image to a large diffusion model, for example, Wonder3D [25], which produces six posed multi-view images of the input shape. Note that, our method is not restricted to specific diffusion model, and we have experimented with Wonder3D and Stable Video Diffusion [2]

(see Tabs. 1 and 2 and Figs. 4 and 5), as a proof of concept. Finally, DepthAnything[46] is exploited to generate corresponding depth images for each view, denoted as I_d^i and I_{cam}^i for the depth image and the camera pose, respectively. The purpose of having depth images is to extract more accurate shape information from the 2.5D images. See our ablation study (Sec. 4.3) on the visual signal selection.

3.2. Multi-modality Shape Fusion

Having the multi-view depth images of the imagined shape, next, the key is to effectively fuse them into a full 3D shape that respects the golden partial observation, while accepting the missing regions from multi-view images. We thus designed a multi-modality shape fusion module with two specialized encoders and a fuser.

Partial Point Cloud Encoder. Due to the nature of single-view scanning, the partial observation is a golden standard for the desired shape, containing global and local geometric priors. We thus adopted a patch-based Transformer encoder to effectively extract geometric features, as shown in Fig. 3 (a). Formally, we first select K seed points from the partial point cloud to divide it into patches $P_{in}^i = \{P_1, P_2, \dots, P_K\}$, based on a fixed radius r . Each patch goes into a DGCNN [38] encoder to extract patch-level features, while the center point P_{center}^i (*i.e.*, the seed point) of each patch is transformed into a positional encoding via

the sinusoidal function. Finally, the Transformer encoder T_P^e takes as input the concatenated features and outputs a unified feature $\mathcal{F}_P \in \mathbb{R}^{128}$ of the partial point cloud after average pooling, defined as:

$$\mathcal{F}_P = \text{AvgPool} \left(T_P^e (\text{concat}(\text{DGCNN}(P_{in}^i), \text{Sins}(P_{center}^i))) \right). \quad (1)$$

Multi-view Image Encoder. Given the posed multi-view depth images, a natural way is to fuse them into 3D and extract features from the fused 3D shape directly. We have proved in the ablation study in Sec. 4.3 that the resulting shape is irregular and noisy, because of the inherent inconsistency of the multi-view generation. To accurately extract global and local shape cues from the images, particularly for the missing regions, while mitigating the impact of inconsistencies, we have designed a patch-based image encoder, as shown in Fig. 3 (b). Specifically, each image I_d^i goes through a pre-trained ResNet backbone to obtain the image feature, while its corresponding camera pose is further encoded via a two-layer MLP to create the positional encoding. Similarly, the Transformer T_I^e takes as input the concatenated feature and produces the final multi-view image fusion feature $\mathcal{F}_I \in \mathbb{R}^{128}$ after average pooling, defined as:

$$\mathcal{F}_I = \text{AvgPool} \left(T_I^e (\text{concat}(\text{ResNet}(I_d^i), \text{MLP}(I_{cam}^i))) \right). \quad (2)$$

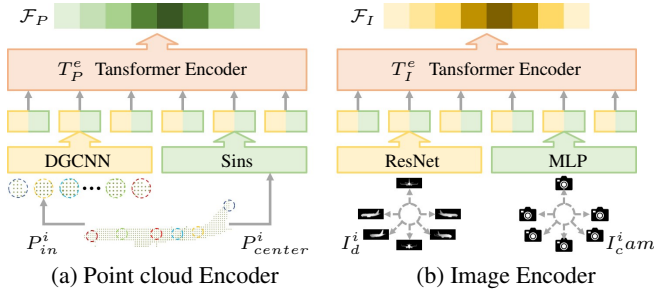


Figure 3. The partial point cloud and multi-view image encoders.

Mutli-modality Fuser. In order to effectively exploit the complementary information in both modalities, we resort to the attention mechanism to fuse the aforementioned features. Formally, we treat the point cloud feature \mathcal{F}_P as the query, while the image feature \mathcal{F}_I as the key and value, defined as:

$$Q = W^Q \mathcal{F}_P, \quad K = W^K \mathcal{F}_I, \quad V = W^V \mathcal{F}_I, \quad (3)$$

where the weights are learnable parameters. Then the attention is calculated as follows:

$$\mathcal{F}_{fusion} = \text{softmax} \left(\frac{QK}{\sqrt{128}} \right) V. \quad (4)$$

A final three-layer MLP converts the fused feature into an initial coarse point cloud P_c .

3.3. Shape Consolidation

Due to the inherent inconsistencies in multi-view depth images and limitations in network fitting capabilities, the predicted coarse point cloud tends to be noisy and with localized holes. To address these issues, we further propose a confidence-based shape consolidator to produce the final dense completed point cloud.

Point Filtering. As shown in Fig. 1 bottom right, we assign confidence scores to each point within P_c by examining 1) the consistency between each point and the multi-view feature \mathcal{F}_I and 2) the intra-agreement between points. Specifically, a point coordinate first goes through an MLP layer to obtain a corresponding feature, which is then concatenated with \mathcal{F}_I , as \mathcal{F}_{com}^i . We then calculate the average self-attention scores among all the concatenated features:

$$Q_{com}^i = W_{com}^Q \mathcal{F}_{com}^i, \quad K_{com}^i = W_{com}^K \mathcal{F}_{com}^i, \quad (5)$$

$$S = \text{Sigmoid} \left(\text{Avg} (\text{dot}(Q_{com}^i, K_{com}^i)) \right).$$

We empirically divided P_c into high and low confidence sets (75% vs. 25%) based on the calculated confidence score, and take the first set as a filtered intermediate point cloud P_f that is significantly regular and compact.

Final Consolidation. Firstly, we simply merge P_f and P_c to become a denser point cloud, then apply farthest point sampling (FPS) to obtain a new point set $P_{de} \in \mathbb{R}^{N \times 3}$. We finally upsample P_{de} to produce the dense and uniformly distributed complete point cloud.

Specifically, we use an MLP to extract per-point shape features (\mathbb{R}^{128}) from P_{de} and point-wise concatenate them with the \mathcal{F}_{fusion} , resulting in a combine feature of dimension \mathbb{R}^{256} . The fused features are then projected to a high-dimensional space to generate a set of offsets $P_{offset} \in \mathbb{R}^{RN \times 3}$ (i.e., R times the number of points), defined as:

$$P_{offset} = \text{MLP} \left(\Re (\text{concat}(\text{MLP}(P_{de}), \mathcal{F}_{fusion})) \right), \quad (6)$$

where $\Re()$ reshapes $\mathbb{R}^{N \times 256}$ to $\mathbb{R}^{RN \times 256/R}$. We then map it to $\mathbb{R}^{RN \times 3}$ by a one-layer MLP. Finally, for each point in P_{de} , we add the R offsets from P_{offset} to produce the final completion result $P_r \in \mathbb{R}^{RN \times 3}$.

Network Training Our whole network is trained end-to-end with the Chamfer distance loss. Specifically, we measure the discrepancy between the ground truth point cloud and the coarse (P_c) and final (P_r) point clouds, respectively. Inspired by [47], we exploit the extra hyperbolic Chamfer distance (HyperCD) to combat noise and outliers, defined as:

$$CD(X, Y) = \frac{1}{|X|} \sum_{x \in X} \min_{y \in Y} \|x - y\|_2 + \frac{1}{|Y|} \sum_{y \in Y} \min_{x \in X} \|x - y\|_2 \quad (7)$$

Table 1. Quantitative results on the PCN dataset. (ℓ^1 CD $\times 10^3$ and F-Score@1%). We show the Chamfer distance for each category while reporting the average on the three metrics on the right. ‘-’ indicates the metric is not applicable, and the **red** and **yellow** colors indicate the best and the second best of the competing methods.

Methods	Plane	Cabinet	Car	Chair	Lamp	Couch	Table	Boat	CD-Avg↓	DCD-Avg↓	F1↑
PCN [49]	5.82	10.91	9.00	11.09	11.91	12.06	9.56	9.12	9.93	-	0.657
GRNet [44]	8.51	12.84	10.17	12.13	11.83	12.64	11.16	9.84	11.14	0.765	0.563
PoinTr [48]	4.31	9.23	7.60	8.35	8.27	9.38	7.97	7.01	7.76	0.562	0.810
PMP-Net++ [40]	4.80	11.70	8.96	8.93	7.04	12.25	8.57	6.88	8.64	0.714	0.683
SnowFlakeNet [43]	3.95	8.82	7.52	7.48	6.34	8.88	6.61	6.10	6.96	0.567	0.828
SeedFormer [55]	3.87	9.05	7.53	7.63	6.12	9.26	6.61	6.03	7.01	0.573	0.824
AnchorFormer [6]	3.62	8.79	7.20	7.12	6.18	8.71	6.50	6.01	6.77	0.539	0.841
HyperCD [21]	3.87	9.05	7.40	7.50	5.95	9.25	6.50	5.89	6.93	-	-
SVDFormer [56]	3.68	8.73	7.10	6.95	5.64	8.58	6.26	5.91	6.61	0.534	0.848
CRA-PCN [30]	3.62	8.77	7.00	6.92	5.46	8.59	6.27	5.86	6.56	-	-
Ours(SVD-MV)	3.51	8.62	6.92	6.91	5.66	8.31	6.27	5.90	6.52	0.531	0.856
Ours(Wonder3D)	3.52	8.72	6.89	6.71	5.64	8.32	6.24	5.84	6.49	0.518	0.859

and

$$\mathcal{L}_{\text{HCD}}(X, Y) = \text{arcosh}(1 + \mathcal{L}_{\text{CD}}(X, Y)), \quad (8)$$

where $\|x - y\|_2^2$ is the Euclidean distance between point x and y . The final loss is:

$$\mathcal{L} = \mathcal{L}_{\text{HCD}}(P_c, G) + \mathcal{L}_{\text{HCD}}(P_r, G). \quad (9)$$

4. Experiments

4.1. Dataset

PCN dataset. The PCN dataset [49] is a subset of the ShapeNet dataset [5], containing shapes from eight categories. In this study, we constructed our dataset based on PCN. Specifically, given the mesh data of a complete object, we selected a fixed viewpoint (the same as the Wonder3D viewpoint) along the positive z-axis on its unit sphere to obtain a single-view depth image and generated a partial point cloud with 2,048 points through a back-projection method. Additionally, multi-view images were produced from the single-view depth image using the multi-view image generation module (Sec. 3.1). We uniformly sampled 16,384 points from the mesh surface to obtain the corresponding ground truth point cloud for each object. In total, we collected 30974 samples and split the dataset into training, validation, and test sets, the ratio is the same as [49].

ShapeNet-55 dataset. Unlike the PCN dataset [49], ShapeNet-55 [48] includes shapes from 55 categories. We apply the same construction method as aforementioned to create a dataset.

Evaluation metrics. Following recent works [55, 56], we adopt Chamfer Distance (CD), Density-aware CD (DCD) [42], and F1-Score as evaluation metrics, and report

the ℓ^1 version of CD for PCN dataset and the ℓ^2 version of CD for Shapenet-55 dataset.

Implementation. Our model is trained for 300 epochs on both datasets using four NVIDIA 4090 GPUs with a batch size of 24. We employ the Adam optimizer with an initial learning rate of $1e^{-4}$. It is decayed by a factor of 0.7 every 40 epochs on the PCN dataset [49] and by a factor of 0.98 every 2 epochs on the ShapeNet-55 dataset [48]. In all of our experiments, we set K to 128 and r to 0.2. For ControlNet, we set the control strength to 1.0 and the guidance scale to 5.0. For Stable Video Diffusion (SVD-MV), we set the elevation angle to 5 degrees, leveraging its strong generalization capability, while keeping all other parameters at their default values. The resulting video contained 21 frames, from which we selected 6 fixed frames as the multi-view images. Finally, we normalized the generated depth image values to the range of 0 to 1.

4.2. Comparisons

To demonstrate the effectiveness of our method, we compare it with SoTA methods, including PCN [49], GRNet [44], PoinTr [48], PMP-Net++ [40], SnowFlakeNet [43], SeedFormer [55], AnchorFormer [6], HyperCD [21], SVDFormer [56], and CRA-PCN [30]. We retrain their networks from scratch on our datasets with their default configurations. The quantitative and qualitative results are presented in the following.

Results on PCN Dataset. The quantitative results in Tab. 1 demonstrate that our method outperforms all previous approaches across nearly all categories while achieving the best average performance. An exception is the *Lamp*, where CRA-PCN achieves slightly better performance. The inconsistency in the multi-view image generation module, especially when the lamp’s support structure has a folding line or curved shape, leads to lower accuracy in our method. A visual comparison is presented in Fig. 4, where the visual re-

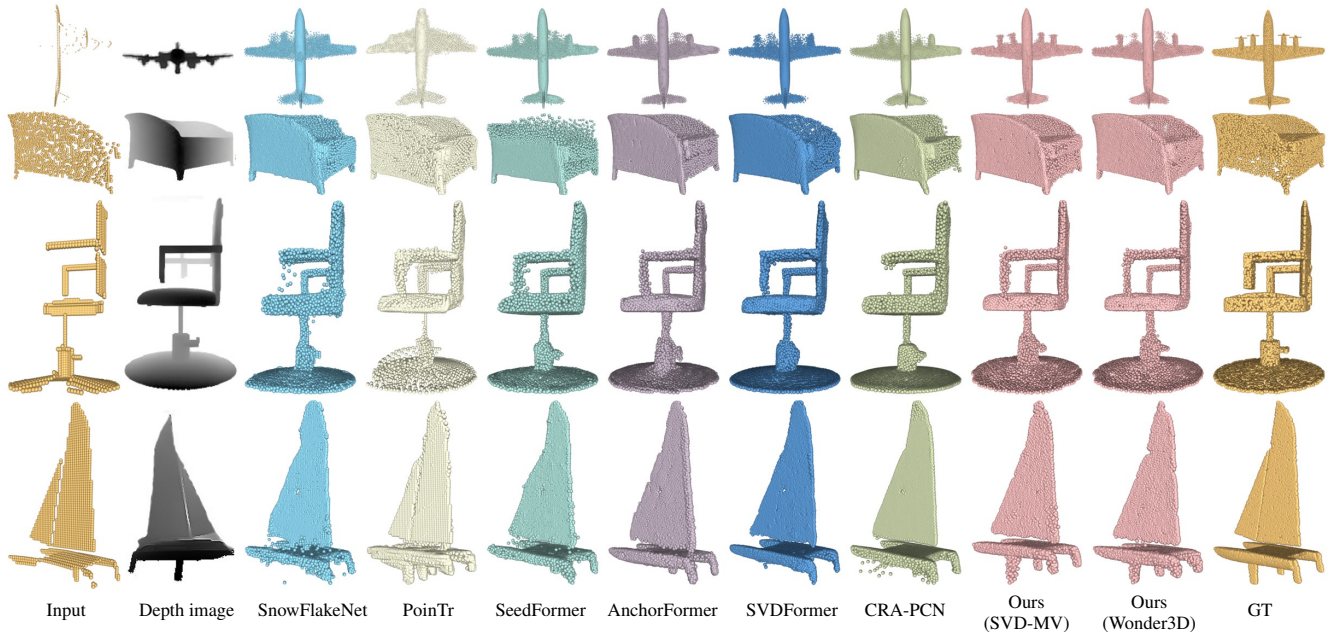


Figure 4. **Visual comparisons on the PCN dataset.** That second column is representative depth images selected from the multiple views.

Table 2. Quantitative results on the ShapeNet-55 dataset (ℓ^2 CD $\times 10^3$ and F-Score@1%). Similarly, Chamfer distance is reported for each category, while the average performance is listed in the right-most columns.

Methods	Table	Chair	Plane	Car	Sofa	Dishwasher	Mailbox	Microwave	Pillow	Remote	CD-Avg↓	DCD-Avg↓	F1↑
PCN [49]	1.80	1.59	0.81	1.44	1.52	1.50	1.73	1.83	1.33	0.78	2.064	0.667	0.194
GRNet [44]	1.72	1.54	0.82	1.56	1.61	1.77	1.39	1.91	1.39	0.79	1.801	0.696	0.243
PoinTr [48]	1.62	1.23	0.86	1.13	1.00	1.00	0.84	1.22	0.73	0.51	1.062	0.643	0.387
AnchorFormer [6]	1.12	0.81	0.43	1.11	0.93	1.21	0.81	1.22	0.71	0.36	1.182	0.670	0.328
SVDFormer [56]	1.03	0.80	0.44	1.00	0.88	1.00	0.76	1.27	0.71	0.34	0.938	0.621	0.447
CRA-PCN [30]	1.58	1.08	0.58	1.24	1.19	1.31	1.18	1.31	0.86	0.45	1.300	-	-
Ours(SVD-MV)	0.99	0.75	0.41	0.99	0.88	0.94	0.61	1.18	0.65	0.34	0.907	0.559	0.408
Ours(Wonder3D)	0.98	0.71	0.40	0.96	0.85	0.98	0.60	1.21	0.62	0.32	0.895	0.569	0.418

sults in several selected categories (*e.g.*, *Plane*, *Chair*, and *Boat*) show that our method can predict the missing parts more accurately due to the additional shape cues provided by the generated multi-view images. Particularly, for the *Airplane* category, all other methods fail to complete the missing symmetric parts (*e.g.*, the engines), while our results are more consistent with the ground truth.

Results on the ShapeNet-55 Dataset. Following existing work [56], we also compare our method against some competitors [6, 30, 44, 48, 49, 56] on the ShapeNet-55 dataset. We did not compare with SeedFormer-based methods [21, 55] because we have observed occasional numerical failure during their training caused by the occurrence of NaN values. As shown in Tab. 2, we selected 10 representative classes from a total of 55 categories to showcase the Chamfer Distance (CD). Our method consistently outperforms other state-of-the-art approaches across all categories, with a particularly notable improvement of 0.16 in the CD metric for the *Mailbox* category. Although the

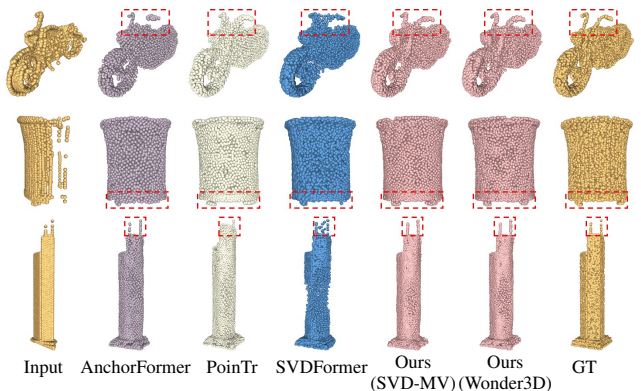


Figure 5. **Visual comparisons on the PCN dataset.** The red-boxed regions highlight the effectiveness of different methods in completing local structures.

first five classes contain significantly more samples than the latter five, we have obtained comparable results across the ten categories, which demonstrates the generalization abil-

Table 3. Effect of applying both partial point cloud and depth images (ℓ^1 CD $\times 10^3$ and F-Score@1%).

Depth images	Partial input	CD-Avg \downarrow	DCD-Avg \downarrow	F1 \uparrow
✓		17.69	0.823	0.401
	✓	6.91	0.534	0.840
✓	✓	6.49	0.518	0.858

ity and robustness of our method on diverse types of data. The visual comparison in Fig. 5 also clearly illustrates the superior performance on more complex shapes with finer details.

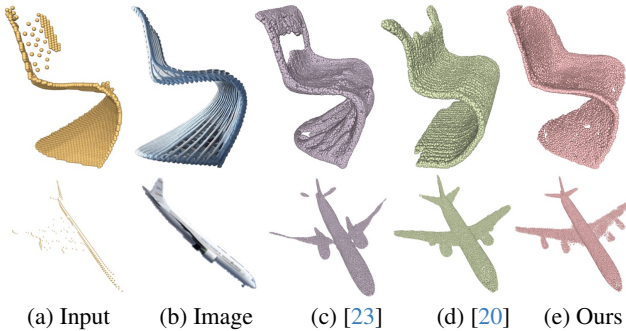


Figure 6. **Visual comparisons with 3D model generation based on single-view RGB image.** (b) shows an RGB image generated by ControlNet from a single-view depth image. (c) One-2-3-45++ [23], (d) Crafsman [20].

Comparison with 3D model generation. We further compare our approach with recent methods [20, 23] that are pre-trained on large-scale datasets and leverage powerful diffusion models to generate complete 3D models from a single-view RGB image, thereby enabling effective shape completion as well. For a fair comparison, we employ ControlNet to generate an RGB image from a single-view depth image, which is then used as input to their pretrained models to predict the complete 3D shape. Finally, the point cloud is extracted using Poisson disk sampling. As shown in Fig. 6, although One-2-3-45++ [23] and Crafsman [20] can generate overall regular shapes, they fail to capture local geometric features, *e.g.*, the back of the chair and the symmetric engines of the airplane, due to the limited cues from the single-view image. Instead, our methods can faithfully recover a full shape with fine details based on the cues from the multi-view images. More comparison results can be found in the supplementary.

4.3. Ablation study

We have extensively ablated our core design choices, and report both the qualitative and quantitative results on the PCN dataset in the following.

Table 4. Ablation on the type of multi-view images (ℓ^1 CD $\times 10^3$ and F-Score@1%).

RGB images	depth images	CD-Avg \downarrow	DCD-Avg \downarrow	F1 \uparrow
✓		6.63	0.530	0.851
	✓	6.49	0.518	0.858
✓	✓	6.59	0.535	0.851

Is depth image a good choice? From the multi-view image generation module, we obtained both the depth and RGB images. The former contains 2.5D information of the underlying geometry, while the latter presents more vivid appearance cues. In this test, we use either the RGB image, the depth image, or their combination as our multi-view signal in the later modules in our pipeline, and present the statistical results in Tab. 4. As can be seen, the depth-only option outperforms others across multiple metrics. The main reason is that the RGB images generated by ControlNet occasionally contain unrealistic artifacts or inconsistencies, which can adversely affect the completion results.

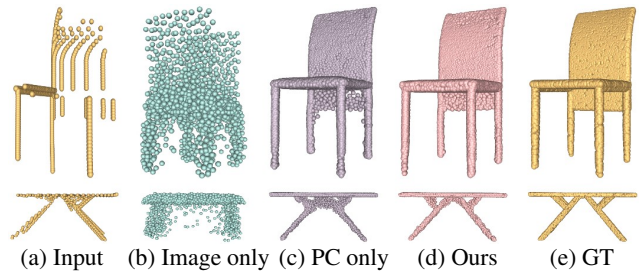


Figure 7. **Visual results of multi-modality fusion.** (b) uses only multi-view images, and (c) uses only the partial point cloud.

Does multi-modality fusion play an important role? To evaluate the effectiveness of our multi-modality fusion strategy, we split the network architecture into two branches. The first branch generates a complete point cloud directly from multi-view images, *i.e.*, after getting \mathcal{F}_I from T_I^e , we use an MLP to map it to a coarse point cloud, which is then refined by the decoder module to produce the final result. The second branch operates solely on the partial point cloud by removing the multi-view image module from our pipeline. Quantitative results of Tab. 3 demonstrate that the multi-modality feature fusion strategy achieves the best performance. As shown in Fig. 7, incorporating additional information from multi-view images allows the model to better capture both the global shape and local structures, such as the backrest of a chair and the supporting regions of a table.

Is confidence filtering helpful? To evaluate the impact of our proposed confidence-based filtering operation, we conducted an ablation study by removing it from our method. As shown in Fig. 8, the red box in (b) highlights noisy points

that are assigned low confidence scores by our method. By applying the filtering strategy, as shown in (c), these noisy points are effectively removed, resulting in a consolidated and improved completion result. Quantitative results in Tab. 5 further demonstrate the effectiveness of the confidence filtering operation.

Table 5. Effect of confidence filtering (ℓ^1 CD $\times 10^3$ and F-Score@1%).

Methods	CD-Avg↓	DCD-Avg↓	F1↑
w/o confidence filtering	6.76	0.525	0.845
Ours	6.49	0.518	0.858

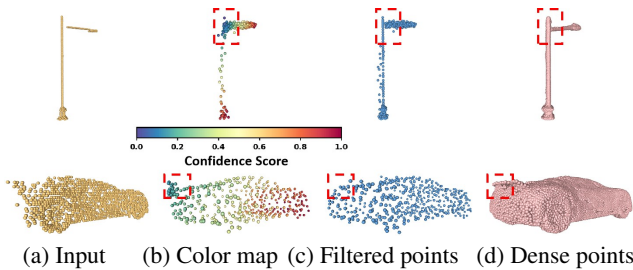


Figure 8. Visualization of confidence filtering.

4.3.1. Discussion

Number of views. The guidance provided by multi-view depth images is crucial for point cloud completion, and the number of views V is a key hyperparameter that significantly affects the results. To investigate, we have conducted a series of experiments. First, the SVD-MV model generates 21 frames for each object. We use this as a candidate set and randomly select $V = 2, 4, 6, 8$ views from it to train the model separately. As shown in Tab. 6, fewer views result in limited coverage of the object’s overall shape. As V increases, the entire shape becomes fully covered, and further increment of V only leads to larger network parameters without significantly improving performance.

Hyperparameters of Filtering. The filtering strategy can effectively reduce noise in the coarse point cloud, thereby improving the accuracy of completion. However, the number of points filtered needs to be carefully balanced. As shown in Tab. 5, filtering too many points can lead to a loss of shape features, affecting the final accuracy, while filtering too few points may retain noise, also impacting precision. To address this, we conducted experiments with different filtering levels and selected the optimal setting.

Limitation. Multi-view depth images can guide point cloud completion, but there are limitations in generating these images. As shown in the Fig. 9, the slender structure of the earphone exhibits significant inconsistencies across different generated views, resulting in poor point cloud completion when used as guidance. In cases like this, where the

Table 6. Number of views (ℓ^1 CD $\times 10^3$ and F-Score@1%).

View number	CD-Avg↓	DCD-Avg↓	F1↑
2	6.65	0.542	0.842
4	6.64	0.539	0.848
6	6.52	0.531	0.856
8	6.62	0.536	0.846

Table 7. Percentage of filtered points (ℓ^1 CD $\times 10^3$ and F-Score@1%).

Filtered points	CD-Avg↓	DCD-Avg↓	F1↑
12%	6.92	0.533	0.840
25%	6.49	0.518	0.858
50%	6.47	0.530	0.857

information visible in a single view is extremely limited, the completion results are often unsatisfactory.

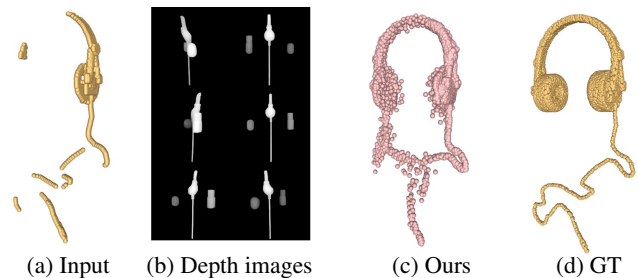


Figure 9. Failure Case. (b) generated inconsistent multi-view depth images.

5. Conclusion

In this paper, we have presented a novel approach for point cloud completion. We, for the first time, introduce diffusion priors in this task to provide imagined full-shape cues for free. From this proof of concept, we believe that diffusion priors can be useful for other point cloud processing tasks, and we hope *PCDreamer* can inspire future research in this direction.

References

- [1] Emanuele Aiello, Diego Valsesia, and Enrico Magli. Cross-modal learning for image-guided point cloud shape completion. *Advances in Neural Information Processing Systems*, 35:37349–37362, 2022. 2
- [2] Andreas Blattmann, Tim Dockhorn, Sumith Kulal, Daniel Mendelevitch, Maciej Kilian, Dominik Lorenz, Yam Levi, Zion English, Vikram Voleti, Adam Letts, et al. Stable video diffusion: Scaling latent video diffusion models to large datasets. *arXiv preprint arXiv:2311.15127*, 2023. 2, 3

- [3] Andreas Blattmann, Robin Rombach, Huan Ling, Tim Dockhorn, Seung Wook Kim, Sanja Fidler, and Karsten Kreis. Align your latents: High-resolution video synthesis with latent diffusion models. In *Proceedings of the IEEE/CVF Conference on Computer Vision and Pattern Recognition*, pages 22563–22575, 2023. 2
- [4] Cesar Cadena, Luca Carlone, Henry Carrillo, Yasir Latif, Davide Scaramuzza, José Neira, Ian Reid, and John J Leonard. Past, present, and future of simultaneous localization and mapping: Toward the robust-perception age. *IEEE Transactions on robotics*, 32(6):1309–1332, 2016. 1
- [5] Angel X Chang, Thomas Funkhouser, Leonidas Guibas, Pat Hanrahan, Qixing Huang, Zimo Li, Silvio Savarese, Manolis Savva, Shuran Song, Hao Su, et al. Shapenet: An information-rich 3d model repository. *arXiv preprint arXiv:1512.03012*, 2015. 5
- [6] Zhikai Chen, Fuchen Long, Zhaofan Qiu, Ting Yao, Wengang Zhou, Jiebo Luo, and Tao Mei. Anchorformer: Point cloud completion from discriminative nodes. In *Proceedings of the IEEE/CVF conference on computer vision and pattern recognition*, pages 13581–13590, 2023. 1, 2, 5, 6
- [7] Angela Dai, Angel X. Chang, Manolis Savva, Maciej Halber, Thomas Funkhouser, and Matthias Nießner. Scannet: Richly-annotated 3d reconstructions of indoor scenes. In *Proc. Computer Vision and Pattern Recognition (CVPR)*, IEEE, 2017. 1
- [8] Angela Dai, Charles Ruizhongtai Qi, and Matthias Nießner. Shape completion using 3d-encoder-predictor cnns and shape synthesis. In *Proceedings of the IEEE conference on computer vision and pattern recognition*, pages 5868–5877, 2017. 2
- [9] Yuwei Guo, Ceyuan Yang, Anyi Rao, Zhengyang Liang, Yaohui Wang, Yu Qiao, Maneesh Agrawala, Dahua Lin, and Bo Dai. Animatediff: Animate your personalized text-to-image diffusion models without specific tuning, 2024. 2
- [10] Yun-Chih Guo, Tzu-Hsuan Weng, Robin Fischer, and Li-Chen Fu. 3d semantic segmentation based on spatial-aware convolution and shape completion for augmented reality applications. *Computer Vision and Image Understanding*, 224: 103550, 2022. 1
- [11] Xiaoguang Han, Zhen Li, Haibin Huang, Evangelos Kalogerakis, and Yizhou Yu. High-resolution shape completion using deep neural networks for global structure and local geometry inference. In *Proceedings of the IEEE international conference on computer vision*, pages 85–93, 2017. 2
- [12] Yingqing He, Tianyu Yang, Yong Zhang, Ying Shan, and Qifeng Chen. Latent video diffusion models for high-fidelity long video generation, 2023. 2
- [13] Hanzhe Hu, Zhizhuo Zhou, Varun Jampani, and Shubham Tulsiani. Mvd-fusion: Single-view 3d via depth-consistent multi-view generation. In *Proceedings of the IEEE/CVF Conference on Computer Vision and Pattern Recognition*, pages 9698–9707, 2024. 2
- [14] Tao Hu, Zhizhong Han, Abhinav Shrivastava, and Matthias Zwicker. Render4completion: Synthesizing multi-view depth maps for 3d shape completion. In *Proceedings of the IEEE/CVF International Conference on Computer Vision Workshops*, pages 0–0, 2019. 2
- [15] Zitian Huang, Yikuan Yu, Jiawen Xu, Feng Ni, and Xinyi Le. Pf-net: Point fractal network for 3d point cloud completion. In *Proceedings of the IEEE/CVF conference on computer vision and pattern recognition*, pages 7662–7670, 2020. 1
- [16] Zehuan Huang, Hao Wen, Junting Dong, Yaohui Wang, Yangguang Li, Xinyuan Chen, Yan-Pei Cao, Ding Liang, Yu Qiao, Bo Dai, et al. Epidiff: Enhancing multi-view synthesis via localized epipolar-constrained diffusion. In *Proceedings of the IEEE/CVF Conference on Computer Vision and Pattern Recognition*, pages 9784–9794, 2024. 2
- [17] Shinpei Kato, Shota Tokunaga, Yuya Maruyama, Seiya Maeda, Manato Hirabayashi, Yuki Kitsukawa, Abraham Monrroy, Tomohito Ando, Yusuke Fujii, and Takuya Azumi. Autoware on board: Enabling autonomous vehicles with embedded systems. In *2018 ACM/IEEE 9th International Conference on Cyber-Physical Systems (ICCP)*, pages 287–296. IEEE, 2018. 1
- [18] Levon Khachatryan, Andranik Movsisyan, Vahram Tadevosyan, Roberto Henschel, Zhangyang Wang, Shant Navasardyan, and Humphrey Shi. Text2video-zero: Text-to-image diffusion models are zero-shot video generators. In *Proceedings of the IEEE/CVF International Conference on Computer Vision*, pages 15954–15964, 2023. 2
- [19] Peng Li, Yuan Liu, Xiaoxiao Long, Feihu Zhang, Cheng Lin, Mengfei Li, Xingqun Qi, Shanghang Zhang, Wenhan Luo, Ping Tan, et al. Era3d: High-resolution multiview diffusion using efficient row-wise attention. *arXiv preprint arXiv:2405.11616*, 2024. 2
- [20] Weiyu Li, Jiarui Liu, Rui Chen, Yixun Liang, Xuelin Chen, Ping Tan, and Xiaoxiao Long. Craftsman: High-fidelity mesh generation with 3d native generation and interactive geometry refiner. *arXiv preprint arXiv:2405.14979*, 2024. 7, 2
- [21] Fangzhou Lin, Yun Yue, Songlin Hou, Xuechu Yu, Yajun Xu, Kazunori D Yamada, and Ziming Zhang. Hyperbolic chamber distance for point cloud completion. In *2023 IEEE/CVF International Conference on Computer Vision (ICCV)*, pages 14549–14560, 2023. 5, 6
- [22] Minghua Liu, Lu Sheng, Sheng Yang, Jing Shao, and Shi-Min Hu. Morphing and sampling network for dense point cloud completion. In *Proceedings of the AAAI conference on artificial intelligence*, pages 11596–11603, 2020. 2
- [23] Minghua Liu, Ruoxi Shi, Linghao Chen, Zhuoyang Zhang, Chao Xu, Xinyue Wei, Hansheng Chen, Chong Zeng, Jiayuan Gu, and Hao Su. One-2-3-45++: Fast single image to 3d objects with consistent multi-view generation and 3d diffusion. In *Proceedings of the IEEE/CVF Conference on Computer Vision and Pattern Recognition*, pages 10072–10083, 2024. 2, 7
- [24] Yuan Liu, Cheng Lin, Zijiao Zeng, Xiaoxiao Long, Lingjie Liu, Taku Komura, and Wenping Wang. Syncdreamer: Generating multiview-consistent images from a single-view image. *arXiv preprint arXiv:2309.03453*, 2023. 2
- [25] Xiaoxiao Long, Yuan-Chen Guo, Cheng Lin, Yuan Liu, Zhiyang Dou, Lingjie Liu, Yuexin Ma, Song-Hai Zhang,

- Marc Habermann, Christian Theobalt, et al. Wonder3d: Single image to 3d using cross-domain diffusion. In *Proceedings of the IEEE/CVF Conference on Computer Vision and Pattern Recognition*, pages 9970–9980, 2024. 2, 3
- [26] Charles R Qi, Hao Su, Kaichun Mo, and Leonidas J Guibas. Pointnet: Deep learning on point sets for 3d classification and segmentation. In *Proceedings of the IEEE conference on computer vision and pattern recognition*, pages 652–660, 2017. 2
- [27] Charles Ruizhongtai Qi, Li Yi, Hao Su, and Leonidas J Guibas. Pointnet++: Deep hierarchical feature learning on point sets in a metric space. *Advances in neural information processing systems*, 30, 2017. 2
- [28] Lingteng Qiu, Guanying Chen, Xiaodong Gu, Qi Zuo, Mutian Xu, Yushuang Wu, Weihao Yuan, Zilong Dong, Liefeng Bo, and Xiaoguang Han. Richdreamer: A generalizable normal-depth diffusion model for detail richness in text-to-3d. In *Proceedings of the IEEE/CVF Conference on Computer Vision and Pattern Recognition*, pages 9914–9925, 2024. 2, 3
- [29] N Dinesh Reddy, Minh Vo, and Srinivasa G Narasimhan. Carfusion: Combining point tracking and part detection for dynamic 3d reconstruction of vehicles. In *Proceedings of the IEEE conference on computer vision and pattern recognition*, pages 1906–1915, 2018. 1
- [30] Yi Rong, Haoran Zhou, Lixin Yuan, Cheng Mei, Jiahao Wang, and Tong Lu. Cra-pcn: Point cloud completion with intra-and inter-level cross-resolution transformers. In *Proceedings of the AAAI Conference on Artificial Intelligence*, pages 4676–4685, 2024. 1, 2, 5, 6
- [31] Yichun Shi, Peng Wang, Jianglong Ye, Mai Long, Kejie Li, and Xiao Yang. Mvdream: Multi-view diffusion for 3d generation. *arXiv preprint arXiv:2308.16512*, 2023. 2
- [32] David Stutz and Andreas Geiger. Learning 3d shape completion from laser scan data with weak supervision. In *Proceedings of the IEEE conference on computer vision and pattern recognition*, pages 1955–1964, 2018. 2
- [33] Junshu Tang, Zhijun Gong, Ran Yi, Yuan Xie, and Lizhuang Ma. Lake-net: Topology-aware point cloud completion by localizing aligned keypoints. In *Proceedings of the IEEE/CVF conference on computer vision and pattern recognition*, pages 1726–1735, 2022. 1
- [34] Jiaxiang Tang, Zhaoxi Chen, Xiaokang Chen, Tengfei Wang, Gang Zeng, and Ziwei Liu. Lgm: Large multi-view gaussian model for high-resolution 3d content creation. In *European Conference on Computer Vision*, pages 1–18. Springer, 2025. 1, 2
- [35] Shitao Tang, Fuyang Zhang, Jiacheng Chen, Peng Wang, and Yasutaka Furukawa. Mvdifffusion: Enabling holistic multi-view image generation with correspondence-aware diffusion. In *Advances in Neural Information Processing Systems*, pages 51202–51233. Curran Associates, Inc., 2023. 2
- [36] Jacob Varley, Chad DeChant, Adam Richardson, Joaquín Ruales, and Peter Allen. Shape completion enabled robotic grasping. In *2017 IEEE/RSJ international conference on intelligent robots and systems (IROS)*, pages 2442–2447. IEEE, 2017. 1, 2
- [37] Xiaogang Wang, Marcelo H Ang Jr, and Gim Hee Lee. Cascaded refinement network for point cloud completion. In *Proceedings of the IEEE/CVF conference on computer vision and pattern recognition*, pages 790–799, 2020. 2
- [38] Yue Wang, Yongbin Sun, Ziwei Liu, Sanjay E Sarma, Michael M Bronstein, and Justin M Solomon. Dynamic graph cnn for learning on point clouds. *ACM Transactions on Graphics (tog)*, 38(5):1–12, 2019. 3
- [39] Zhengyi Wang, Yikai Wang, Yifei Chen, Chendong Xiang, Shuo Chen, Dajiang Yu, Chongxuan Li, Hang Su, and Jun Zhu. Crm: Single image to 3d textured mesh with convolutional reconstruction model. *arXiv preprint arXiv:2403.05034*, 2024. 2, 1
- [40] Xin Wen, Peng Xiang, Zhizhong Han, Yan-Pei Cao, Pengfei Wan, Wen Zheng, and Yu-Shen Liu. Pmp-net++: Point cloud completion by transformer-enhanced multi-step point moving paths. *IEEE Transactions on Pattern Analysis and Machine Intelligence*, 45(1):852–867, 2022. 1, 2, 5
- [41] Lintai Wu, Qijian Zhang, Junhui Hou, and Yong Xu. Leveraging single-view images for unsupervised 3d point cloud completion. *IEEE Transactions on Multimedia*, 2023. 1, 2
- [42] Tong Wu, Liang Pan, Junzhe Zhang, Tai Wang, Ziwei Liu, and Dahua Lin. Balanced chamfer distance as a comprehensive metric for point cloud completion. *Advances in Neural Information Processing Systems*, 34:29088–29100, 2021. 5
- [43] Peng Xiang, Xin Wen, Yu-Shen Liu, Yan-Pei Cao, Pengfei Wan, Wen Zheng, and Zhizhong Han. Snowflakenet: Point cloud completion by snowflake point deconvolution with skip-transformer. In *Proceedings of the IEEE/CVF international conference on computer vision*, pages 5499–5509, 2021. 1, 2, 5
- [44] Haozhe Xie, Hongxun Yao, Shangchen Zhou, Jiageng Mao, Shengping Zhang, and Wenxiu Sun. Grnet: Gridding residual network for dense point cloud completion. In *European conference on computer vision*, pages 365–381. Springer, 2020. 5, 6
- [45] Xuejun Yan, Hongyu Yan, Jingjing Wang, Hang Du, Zhihong Wu, Di Xie, Shiliang Pu, and Li Lu. Fbnet: Feedback network for point cloud completion. In *European Conference on Computer Vision*, pages 676–693. Springer, 2022. 1
- [46] Lihe Yang, Bingyi Kang, Zilong Huang, Xiaogang Xu, Jiashi Feng, and Hengshuang Zhao. Depth anything: Unleashing the power of large-scale unlabeled data. In *Proceedings of the IEEE/CVF Conference on Computer Vision and Pattern Recognition*, pages 10371–10381, 2024. 3
- [47] Jinpeng Yu, Binbin Huang, Yuxuan Zhang, Huaxia Li, Xu Tang, and Shenghua Gao. Geformer: Learning point cloud completion with tri-plane integrated transformer. In *ACM Multimedia 2024*. 4
- [48] Xumin Yu, Yongming Rao, Ziyi Wang, Zuyan Liu, Jiwen Lu, and Jie Zhou. PointR: Diverse point cloud completion with geometry-aware transformers. In *Proceedings of the IEEE/CVF international conference on computer vision*, pages 12498–12507, 2021. 1, 2, 5, 6
- [49] Wentao Yuan, Tejas Khot, David Held, Christoph Mertz, and Martial Hebert. Pcn: Point completion network. In *2018 in-*

- ternational conference on 3D vision (3DV)*, pages 728–737. IEEE, 2018. [1](#), [2](#), [5](#), [6](#)
- [50] Lvmin Zhang, Anyi Rao, and Maneesh Agrawala. Adding conditional control to text-to-image diffusion models. In *Proceedings of the IEEE/CVF International Conference on Computer Vision*, pages 3836–3847, 2023. [3](#)
- [51] Xuancheng Zhang, Yutong Feng, Siqi Li, Changqing Zou, Hai Wan, Xibin Zhao, Yandong Guo, and Yue Gao. View-guided point cloud completion. In *Proceedings of the IEEE/CVF conference on computer vision and pattern recognition*, pages 15890–15899, 2021. [1](#), [2](#)
- [52] Yabo Zhang, Yuxiang Wei, Dongsheng Jiang, Xiaopeng Zhang, Wangmeng Zuo, and Qi Tian. Controlvideo: Training-free controllable text-to-video generation. *arXiv preprint arXiv:2305.13077*, 2023. [2](#)
- [53] Hengshuang Zhao, Li Jiang, Jiaya Jia, Philip HS Torr, and Vladlen Koltun. Point transformer. In *Proceedings of the IEEE/CVF international conference on computer vision*, pages 16259–16268, 2021. [2](#)
- [54] Daquan Zhou, Weimin Wang, Hanshu Yan, Weiwei Lv, Yizhe Zhu, and Jiashi Feng. Magicvideo: Efficient video generation with latent diffusion models. *arXiv preprint arXiv:2211.11018*, 2022. [2](#)
- [55] Haoran Zhou, Yun Cao, Wenqing Chu, Junwei Zhu, Tong Lu, Ying Tai, and Chengjie Wang. Seedformer: Patch seeds based point cloud completion with upsample transformer. In *European conference on computer vision*, pages 416–432. Springer, 2022. [1](#), [2](#), [5](#), [6](#)
- [56] Zhe Zhu, Honghua Chen, Xing He, Weiming Wang, Jing Qin, and Mingqiang Wei. Svdformer: Complementing point cloud via self-view augmentation and self-structure dual-generator. In *Proceedings of the IEEE/CVF International Conference on Computer Vision*, pages 14508–14518, 2023. [1](#), [2](#), [5](#), [6](#)

PCDreamer: Point Cloud Completion Through Multi-view Diffusion Priors

Supplementary Material

In this supplementary, we present more visual results on the PCN [49] and ShapeNet-55 [48] datasets. We also present additional visual examples, comparing our approach against more single-view 3D generation methods. Besides, to further demonstrate the generalization ability of our method in real-world scans, we also conduct experiments on the ScanNet dataset [7], which contains partial point clouds extracted from RGB-D scans.

Additional results on Real-world Scans. We evaluated our method on real-world scanned data from the ScanNet dataset [7] to assess its performance. Specifically, we selected depth images of individual objects and their corresponding partial point clouds from ScanNet. Using our multi-view generation module, we obtained multi-view depth images. These were then input into our model, which was pre-trained on the PCN dataset, to produce the completion results. As shown in Fig. 1, our method yields reasonable and high-quality results on real scanned data, demonstrating its effectiveness and robustness in handling real-world inputs.

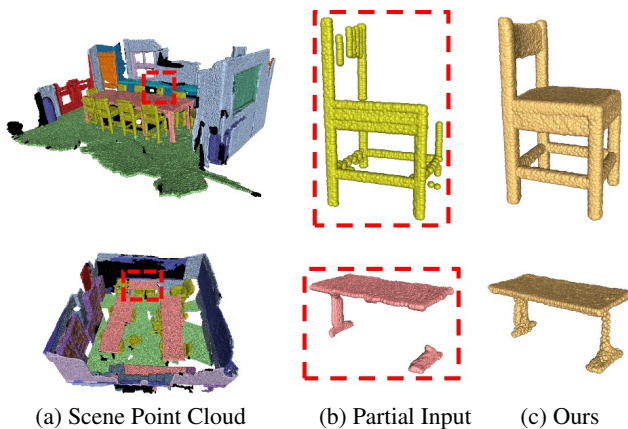


Figure 1. Visual results on real world scans.

Visual comparison. In Fig. 2, we present additional comparisons with other 3D model generation methods [34, 39]. Moreover, we provide further examples from the PCN dataset for comprehensive evaluation. As illustrated in the figure, the lack of extra views, the randomness in the generation process, and the inherent inconsistencies in multi-view images often prevent single-view 3D model generation methods from effectively capturing geometric details. Consequently, these models may produce shapes that, while plausible, exhibit significant deviations from the ground

truth, such as variations in the width of the sofa. Therefore, multi-view images are more appropriate as auxiliary cues for point cloud completion, although directly utilizing them for point cloud completion typically yields suboptimal results.

Additional results on PCN and ShapeNet-55 dataset.

Figs. 3 and 4, each presents an extra six results from the PCN and the ShapeNet-55 datasets, respectively. For both datasets, the first three cases in the first three rows possess high-quality and consistent multi-view depth images, whereas depth images with lower quality and less consistency are generated for the last three examples. Specifically, the high randomness of the generation process, combined with limitations of the initial view, can result in multi-view depth images exhibiting inconsistencies across views (*e.g.*, the lid of the *Dustbin*), missing geometric details (*e.g.*, the *Helmet*), and the presence of noisy regions (*e.g.*, the leg of the *Table*). Furthermore, shapes imagined by the generative model may exhibit scale discrepancies relative to their real-world counterparts (*e.g.*, the *Sofa* and the *Table*). In addition, the depth estimation process may also occasionally produce suboptimal outcomes (*e.g.*, the *Dishwasher*). However, the proposed confidence-based shape consolidator effectively addresses these issues by eliminating unreliable points caused by inconsistencies in diffusion priors. As a result, our models produce accurate and reasonable outputs, as demonstrated in the second and fourth columns of the last three examples.

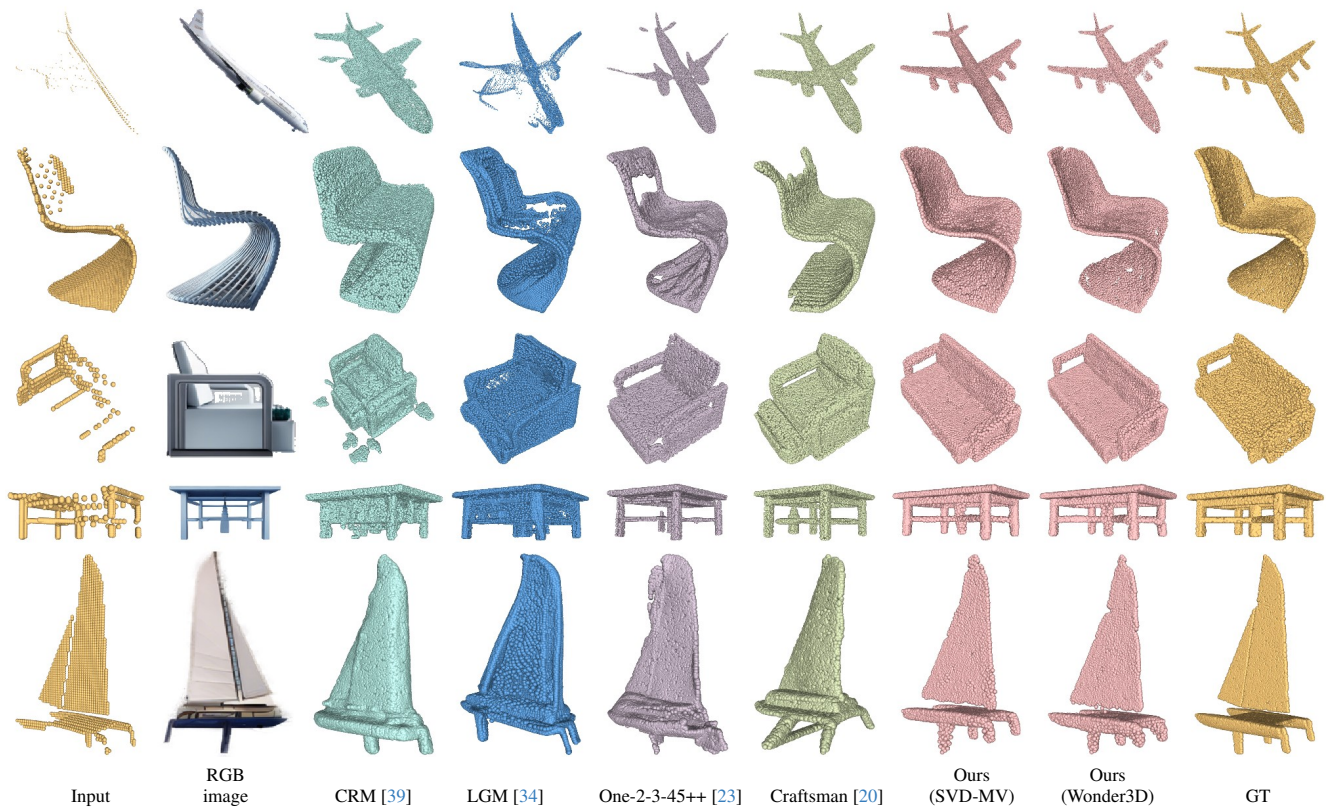


Figure 2. Additional visual comparisons with 3D model generation based on single-view RGB image.

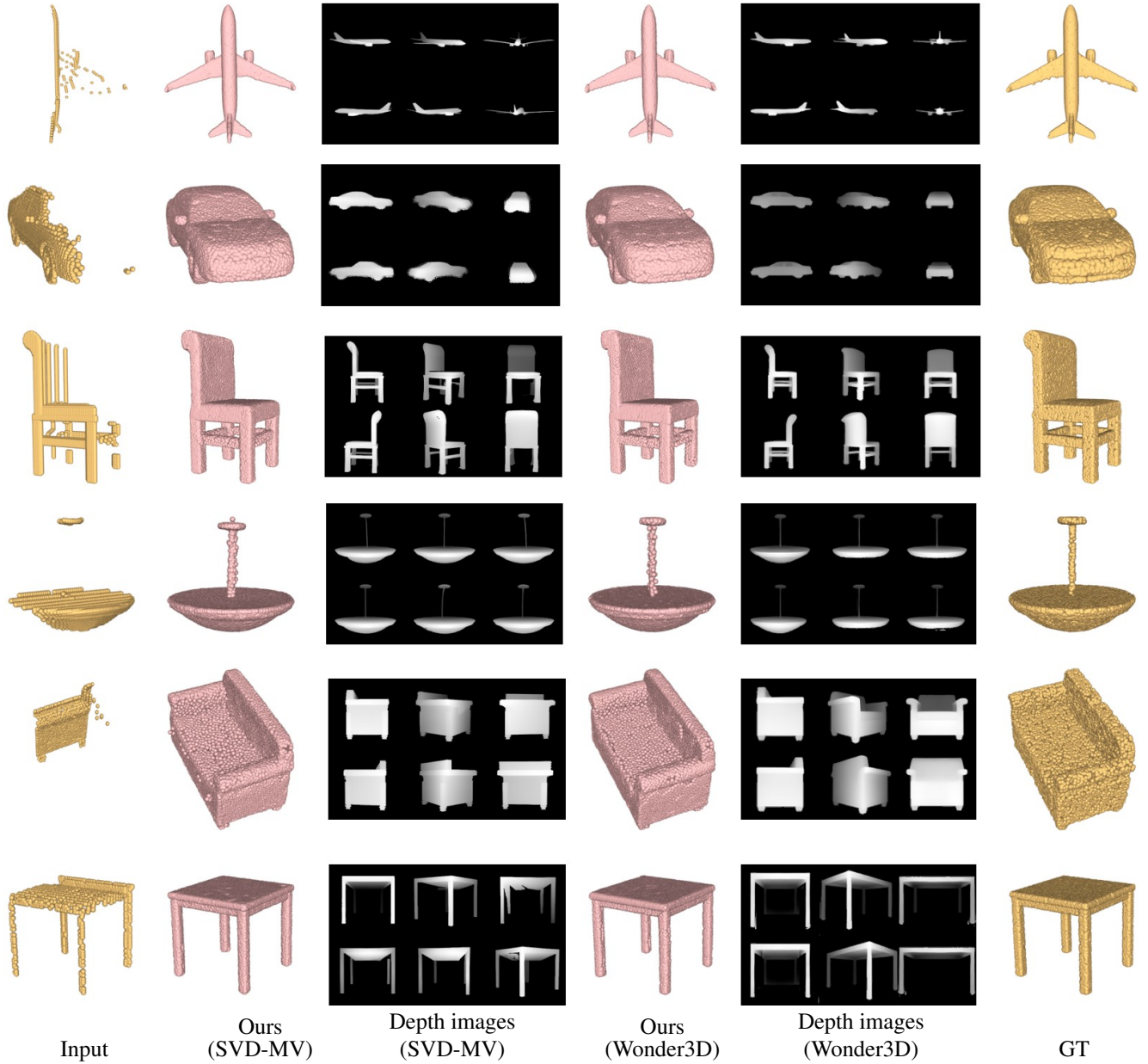


Figure 3. **Visual results as well as multi-view depth images on the PCN dataset.** The generated multi-view depth images corresponding to the last three rows exhibit lower quality and less consistency than the first three rows.

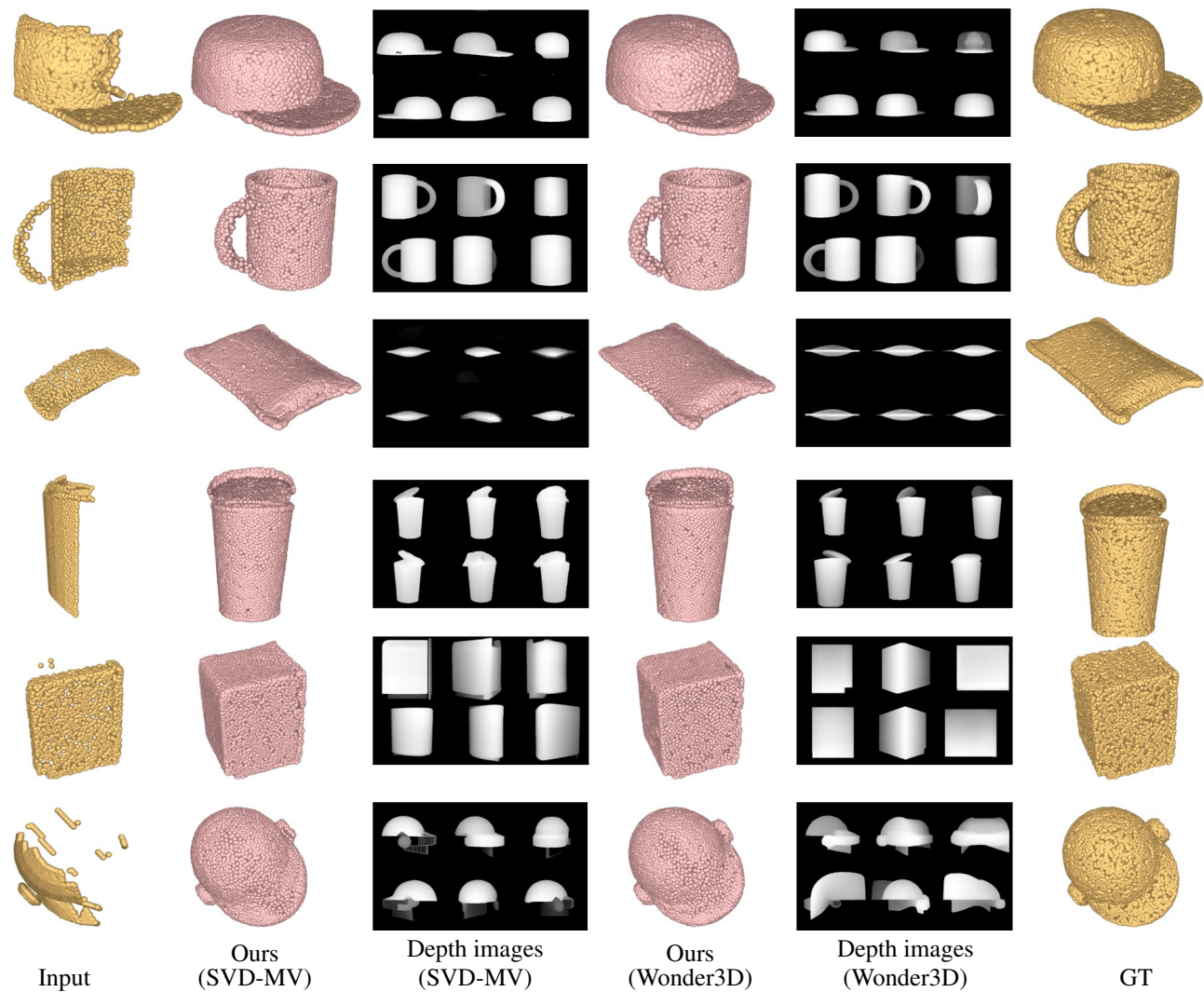


Figure 4. **Visual results as well as multi-view depth images on the ShapeNet-55 dataset.** The generated multi-view depth images corresponding to the last three rows exhibit lower quality and less consistency than the first three rows.